

**USGS Award Number 05HQGR0111:****MODELLING AND SEISMOLOGICAL STUDIES OF PROCESS AND HAZARD OF  
CASCADIA IN-SLAB EARTHQUAKES (Final Report)**

K. Wang, H. Kao, J. F. Cassidy  
Pacific Geoscience Centre, Geological Survey of Canada  
9860 W Saanich Rd, Sidney, B. C., Canada V8L 4B2

Phone: (250)363-6429; Fax: (250)363-6565; Email: Kwang@nrcan.gc.ca

URL: <http://www.pgc.nrcan.gc.ca>

Element Designation: I and II, Pacific Northwest

Key Words: Thermophysical modeling, Fault stress interactions, Wave propagation, Source characteristics

**Abstract.** In assessing hazards due to intraslab earthquakes at Cascadia, one important question is whether the maximum size of these events is limited by geological structure. We address this question in this project by studying the rupture process of the M6.8 2001 Nisqually earthquake. We modify the source-scanning algorithm, originally developed for the purpose of locating non-volcanic seismic tremors, and use it to determine the rupture plane and history of this event. The method does not make any a priori assumption on the geometry of the rupture. Our results reveal that the rupture fault of the Nisqually earthquake steeply dips east, indicating that the nearly vertical one of the two focal planes determined from moment tensor inversion is the rupture plane. The rupture initiated near the subducting Moho and propagated downward, and therefore it must have significantly involved the subducting mantle. This indicates that the Cascadia intraslab earthquakes are not confined in the dehydrating subducting crust, so that their maximum size is not limited by the about 7 km thickness of the crust.

**Introduction**

Most of the seismic hazard in the Pacific Northwest over the past century has been caused by earthquakes that occur within the young subducted Juan de Fuca (JDF) plate in a depth range of 40 – 80 km. The most recent example of these damaging events is the M 6.8 2001 Nisqually earthquake. Traditionally, hazard assessment for these events has been based primarily on statistical analyses of historical earthquakes, but recent progresses in slab-earthquake research have provided the possibility of adding a physics-based approach. A conceptual breakthrough over the past few decades is the recognition that intermediate-depth intraslab earthquakes are associated with dehydration of the subducting slab.

Dehydration of hydrous minerals in the slab may raise pore fluid pressure to near-lithostatic values to facilitate brittle failure, a process called dehydration embrittlement. Without elevated fluid pressure, rock failure under the tremendous in situ confining pressure of the slab environment is expected to be aseismic, either as cataclastic flow if the temperature is low or as

plastic creep if the temperature is high [Stöckhert and Renner, 1998]. Although it is the tectonic stress that ultimately causes failure, dehydration embrittlement provides a condition for the failure to occur as earthquakes.

Most of the bonded  $H_2O$  in the oceanic lithosphere is in the highly fractured basaltic-gabbroic crust. It is thus expected that intraslab earthquakes occur mostly in the dehydrating subducting crust, as a result of reactivation of preexisting faults destabilized by metamorphic fluids [Kirby et al., 1996; Peacock and Wang, 1999]. If this is the case, then the size of intraslab events may be limited by the thickness of the subducting crust. Intraplate earthquake ruptures do not have large aspect ratios (length/width), so that a limit to any length dimension is also a limit to the size of the rupture area and hence the seismic moment. On the other hand, there is reason to expect intraslab earthquakes to occur also in the slab mantle. Except near the mid-ocean ridges, the uppermost part of the oceanic mantle, even for a very young and warm plate like the Juan de Fuca plate, is under a pressure and temperature condition in which serpentine is stable. The serpentine will dehydrate during slab subduction [Hacker et al., 2003] and may lead to dehydration embrittlement, facilitating earthquakes in the subducting mantle. The possibility of significant mantle involvement in intraslab earthquakes is debatable because of the question whether there is enough  $H_2O$  below the oceanic Moho thus a sufficient degree of serpentinization prior to subduction.

The most direct approach to resolving the issue of mantle involvement in intraslab earthquakes is to study rupture geometry of past intraslab earthquakes. The best recorded large intraslab event at Cascadia is the 2001 Nisqually earthquake of M 6.8. The hypocenter of the Nisqually earthquake is located at a depth of 54 km, near the Moho discontinuity of the

subducted plate (Fig. 1a). Source mechanisms determined by both the U.S. Geological Survey (USGS) and the Seismological Lab of Harvard University show one nodal plane steeply dipping east and the other shallowly dipping west (Fig. 1a).

If the rupture was on the shallowly west-dipping nodal plane, the entire rupture could barely fit in the slab crust (Fig. 1a), but if it was on the steeply east-dipping plane, it must have extended into the slab mantle [Creager et al., 2002] (Fig. 1a). Specifically, if the steeply east-dipping plane is taken as the rupture plane, inversion of strong motion data shows that the rupture must have propagated downward and that the strongest asperity is located 3–6 km down from the hypocenter, well below the Moho [Ichinose et al., 2004]. However, strong motion data and geodetic data cannot resolve which of the two nodal planes was the rupture plane

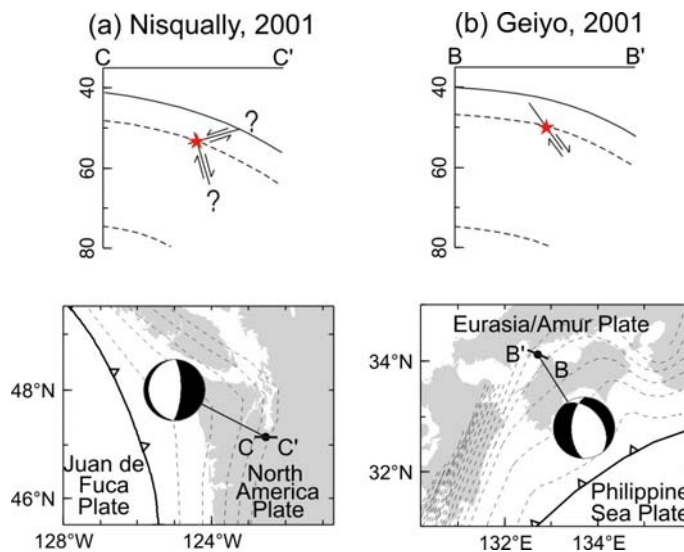


Fig. 1. The Nisqually (a) and Geiyo (b) earthquakes. Focal planes are shown in lower hemisphere projection. For each event, the cross-section along the profile shown on the map illustrates the approximate position of the rupture plane(s) relative to the slab surface and Moho. Slab surface is contoured at 10 km interval (dashed lines). Modified from Wang et al. [2004a].

[Xu et al., 2002; Bustin et al., 2004; Ichinose et al., 2004]. The issue of mantle involvement thus remained unresolved.

A month after the Nisqually earthquake, the 2001 Geiyo earthquake (Fig.1b) occurred within the subducting slab at the Nankai, SW Japan, subduction zone, with a similar magnitude (M 6.7), focal depth, focal mechanism, and site-effect-corrected ground-motion characteristics [Atkinson and Casey, 2002]. Both the Nisqually and Geiyo ruptures started from the base of the slab crust [Creager et al., 2002; Ohkura and Seno, 2002; Kakehi, 2004]. Numerous aftershocks allow the rupture plane of the Geiyo event to be defined, and it clearly extended into the subducting mantle. The Geiyo and Nisqually earthquakes occurred in very similar thermo-tectonic environments [Wang et al., 2004b], and hence the Geiyo case supports the possibility that the Nisqually rupture may also involve the slab mantle. However, the Nisqually earthquake was followed by very few aftershocks in the source region, thus making the identification of the rupture plane very difficult.

In this project, we have constrained the Nisqually rupture plane using the Source-Scanning-Algorithm (SSA). In the original proposal for a two-year project, we also proposed to carry out modeling studies to improve our understanding of the thermal, petrological, and mechanical states of Cascadia intraslab earthquakes. Only the SSA component was approved and funded, and the project was shortened to one year.

## Method Development

The SSA was originally designed to identify seismic sources with emergent arrivals, such as the low-frequency nonvolcanic tremors in episodic tremor-and-slip (ETS) events in northern Cascadia [Kao and Shan, 2004]. Here, we describe how we have modified the SSA to suit the purpose of the present study.

The SSA identifies seismic sources by systematically scanning the entire model space for ‘bright’ spots. The ‘brightness’ of a given point in space ( $\eta$ ) at a specific time ( $\tau$ ) is defined as

$$br(\eta, \tau) = \frac{1}{N} \sum_{n=1}^N |u_n(\tau + t_{\eta n})| \quad (1)$$

where  $u_n$  is the normalized seismogram amplitude recorded at station  $n$ , and  $t_{\eta n}$  is the predicted travel time from point  $\eta$  to station  $n$  of a particular phase (for locating seismic tremors, we use the  $S$  phase).

In practice, however, our imperfect knowledge of the velocity model used for  $t_{\eta n}$  calculation may cause a slight difference between the predicted and observed arrival times at each station. Therefore, instead of using only the amplitude  $u_n(\tau + t_{\eta n})$  at the predicted arrival time, we modify equation (1) to include a contribution from surrounding points within a chosen time window, such as

$$br(\eta, \tau) = \frac{1}{N} \sum_{n=1}^N \left\{ \frac{\sum_{m=-M}^M W_m |u_n(\tau + t_{\eta n} + m\delta t)|}{\sum_{m=-M}^M W_m} \right\} \quad (2)$$

where  $2M$  is the number of samples within the time window centred around the predicted arrival time,  $\delta t$  is the sampling interval, and  $W_m$  is a weighting factor dependent on the time difference between the observed and predicted arrivals.

In applying the SSA to identify an earthquake’s rupture, the original formulation (i.e.,

equations 1 and 2) becomes less appropriate for two reasons. First, unlike most tremors that are relatively small with a short duration, the source configuration of an earthquake can be much more complicated in both time and space such that points with less brightness cannot be totally ignored. Second, structure-related signals (e.g., coda waves, reflection/refraction from discontinuities, and/or diffracted phases) may be mixed with the source signals to cause false images.

To overcome the first problem, it is necessary to introduce a priori constraints on the earthquake's source. This can be done by adding a station correction term to equation (2) such that the predicted arrivals of source phases are perfectly aligned with the observed ones. As for the second problem, there are at least two ways of remedy. For examples, we can expand the brightness function (equation 2) to include multiple phases, or we can carefully select waveform segments that are relatively free of structure-related phases. While the former approach has the potential to significantly increase the image's resolution, it depends even more heavily on the accuracy of the velocity model. For the latter approach to work, the  $P$  wave trains at stations within a certain distance range seem to form the best datasets. The epicentral distance must be large enough to ensure adequate separation between  $P$  and  $S$  wave trains (that must take the source duration into account), yet sufficiently small to avoid contamination from phases refracted from high velocity zones at depth. In this study, we choose the latter approach because of its simplicity and robustness when an imperfect velocity model is used.

Because each source pulse (assumed to slip only in one direction) propagates through the elastic media in the form of a wavelet (that oscillates between peaks and troughs as governed by the wave equation), another necessary modification is to use waveform envelopes instead of the absolute amplitudes of  $P$  wave trains in the calculation of brightness [Baker et al., 2005]. In other words, the brightness function for imaging an earthquake's rupture configuration is redefined as

$$br(\eta, \tau) = \frac{1}{N} \sum_{n=1}^N \left\{ \frac{\sum_{m=-M}^M W_m |U_n(\tau + t_{\eta n} + m\delta t + t_n^{corr})|}{\sum_{m=-M}^M W_m} \right\} \quad (3)$$

where  $U_n$  is the normalized waveform envelope of the  $P$  wave train recorded at station  $n$ , and  $t_n^{corr}$  is the time correction (i.e., the observed arrival time of the  $P$  phase minus the predicted) for station  $n$ .

Our method is schematically illustrated in Fig. 2. The large white star (S1) marks the centroid of an earthquake where the largest burst of seismic energy is released. Minor bursts are emitted from locations along the rupture plane dipping to the right, as marked by the two smaller gray stars (S2 and S3). The black stars (S4 and S5) are located on the left-dipping auxiliary plane that emits no seismic energy. Above each station are the corresponding waveform envelopes where the predicted arrival times from S1–S5 are labelled. By summing the observed amplitudes at all stations for each star, it is expected to have the brightest spot at S1. S2 and S3 would show some brightness, whereas S4 and S5 are dark due to the lack of observed amplitudes at their respectively predicted arrival times. By systematically calculating the brightness function for all grid points in the source volume, we are able to image the distribution of significant seismic sources (i.e., those responsible for the big energy bursts recorded on seismograms), thus distinguish the rupture plane from the auxiliary one. Similarly, if the rupture process is of long duration, the entire model space can be scanned at a series of time steps, giving the apparent image of rupture propagation. Results of controlled experiments with synthetic data are given in the Appendix.

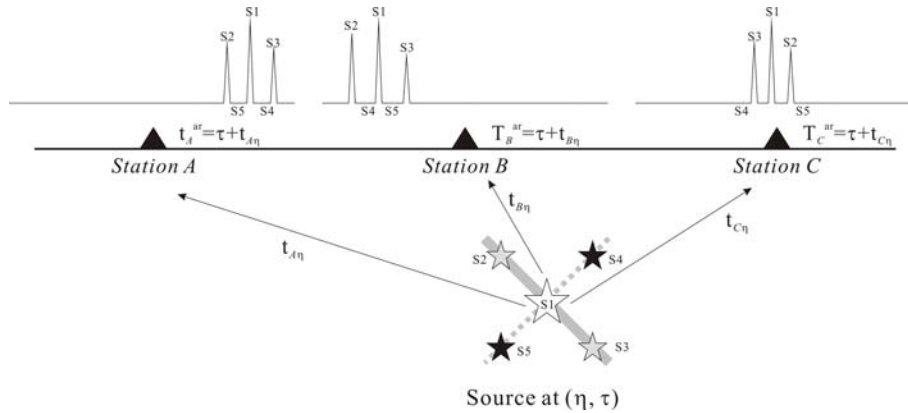


Figure 2. A schematic diagram illustrating how the SSA identifies the rupture plane of an earthquake. Assuming a source at the location  $\eta$  and the time  $\tau$ , SSA calculates the travel times from this source to all stations ( $t_{A\eta}$ ,  $t_{B\eta}$ , and  $t_{C\eta}$ ). The observed waveform amplitudes at the predicted arrival times of all stations ( $t_A^{ar}$ ,  $t_B^{ar}$ ,  $t_C^{ar}$ ) are summed to give the source's 'brightness.' The envelopes of synthetic waveforms, shown at the top, correspond to a rupture dipping to the right (solid line) with the major burst of energy coming from the centroid (S1, white star) and two minor bursts from the updip and downdip edges (S2 and S3, gray stars). There are no significant amplitudes at the predicted arrival times from locations along the auxiliary planes (dashed line, S4 and S5), resulting in little brightness (black stars).

## Imaging the Nisqually rupture

Seismic waveform data are selected from stations of the Pacific Northwest Seismograph Network (PNSN) operated by the University of Washington (Fig. 3). The waveforms are first

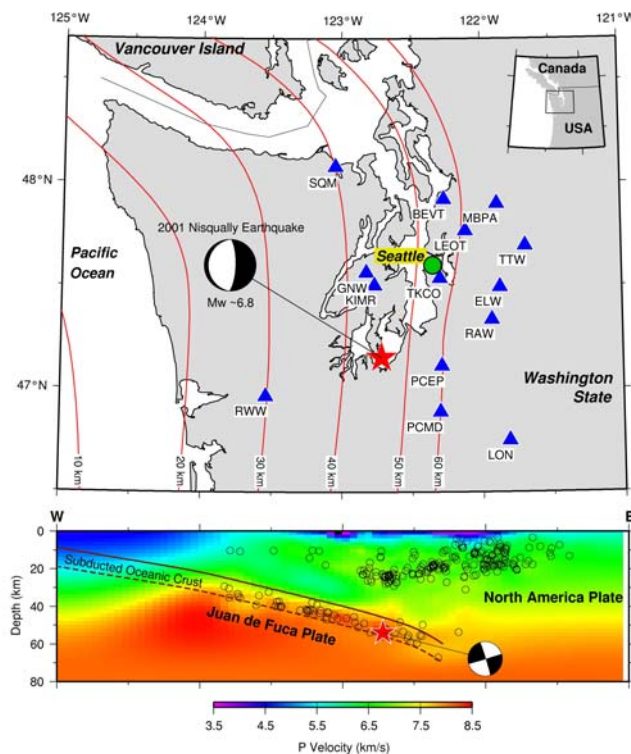


Fig. 3. Upper: Locations of seismic stations used for this study (blue triangles). Red lines are contours of depth to the surface of the slab. Red star shows the epicentre of the Nisqually earthquake, with its focal mechanism indicated by the beach ball. Lower: East-west cross section at the latitude of the Nisqually earthquake, showing the hypocenter (side-view beach ball), other earthquakes (circles), and the slab. The P-wave velocity distribution was determined by Preston et al. [2004].

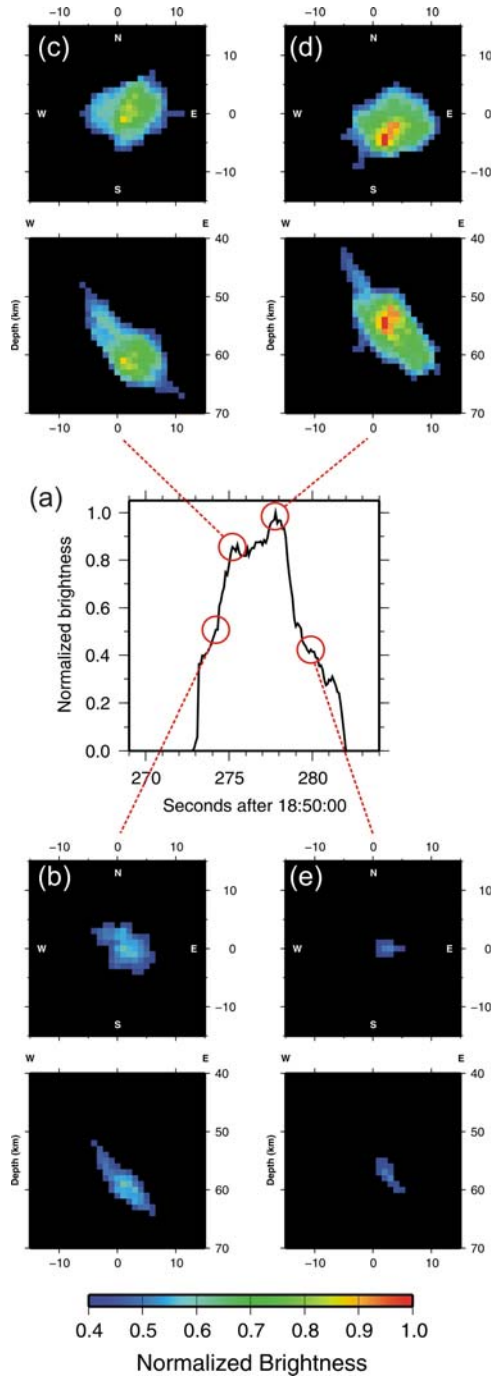


Fig. 4. SSA images of Nisqually rupture. (a): Maximum brightness as a function of time. (b) through (e): Snapshots of the SSA image at time steps as indicated in (a). For each snapshot, the upper panel shows the plan view of the image, and the lower panel shows the side view (from south).

high-pass filtered at 1 Hz to enhance the phases associated with individual sources. The *P* wave trains are extracted and normalized to yield waveform envelopes that are used for source scan. A 3D velocity model derived from regional tomography [Preston et al., 2003] is used in calculating the theoretical travel times. Station corrections (i.e., the time difference between the theoretical and observed first arrival times) are applied during the scanning process. The results of our analysis are shown in Fig. 4.

The maximum brightness value began to increase sharply after the event's origin time (18:54:32.8, Fig. 4a). Because the brightness function is effectively the summation of observed amplitudes at the predicted arrival times of all stations, a patch of greater brightness represents a source of relatively large seismic moment release. The time sequence of the maximum brightness clearly exhibits two peaks separated by  $\sim 2.2$  s (Fig. 4a), and the second peak is stronger than the first one. The source process lasted for  $\sim 6$ – $7$  s if we set the brightness threshold at 0.4 (the brightness value corresponding to *P* wave coda). These spatial and temporal source features are generally consistent with those based on waveform inversion [Ichinose et al., 2004].

Brightness images of the source for a series of time steps collectively depict the orientation of the rupture (Figs. 4b–e). The centroid of the rupture propagated deeper ( $\sim 61$  km) during the initial 2.5 s (Fig. 4b and 4c). At  $\sim 5.5$  s into the rupture process, another strong source was observed  $\sim 6$  km to the south at the depth of the initial rupture (i.e.,  $\sim 54$  km as determined from first arrivals at local networks; Fig. 4d). The source image became barely resolvable soon after (Fig. 4e). Although the brightness function varies significantly in both time and space, the overall oval-shaped pattern dipping steeply to the east remains unchanged throughout the rupture history.

Because of averaging over the finite time window  $\delta t$  of each time step and because of uncertainties in the 3D velocity structure, a rupture plane cannot be imaged as a sharp planar feature. However, it is important to recognize that this smearing effect does not subdue our ability to identify which of the two known nodal planes is the rupture plane. If the shallowly west-dipping plane were the rupture plane, the SSA would yield an elongated cloud of brightness with a distinctly west-dipping orientation, as is shown by the controlled experiments described in the



Appendix. The strength of the SSA method is its independence of any prior assumptions about the rupture plane, and the weakness is the limited resolution. In contrast, the strength of synthetic waveform methods such as strong-motion data inversion is a much better resolution, but the weakness is that a fault plane must be assumed a priori. Now that we have verified that the steeply east-dipping plane is the rupture plane, we can rely on published inversion results based on this assumption [Ichinose et al., 2004] with confidence.

In order to confirm the east-dipping nature of the fault zone, we calculated using forward modeling the predicted arrival times from various locations in the source volume and compared the results to the observed waveform amplitudes. Fig. 5 shows two examples that correspond to different stages of the rupture (Fig. 4b and 4d). For both cases, the centroid locations (stars in Fig. 5) are generally associated with local peaks in most of the waveforms, as marked by the orange lines. The predicted arrival times from locations located downdip along the east-dipping plane (i.e., circles on the cross sections in Fig. 5) and from locations outside of the fault plane (triangles) are marked with green and blue lines, respectively. In general, waveform amplitudes corresponding to locations on the east-dipping plane are relatively larger than those corresponding to locations off the plane. Taking the source image at 277.8 s for example (Fig. 5b), the normalized average amplitude (i.e., brightness) drops by almost 60% if the source is

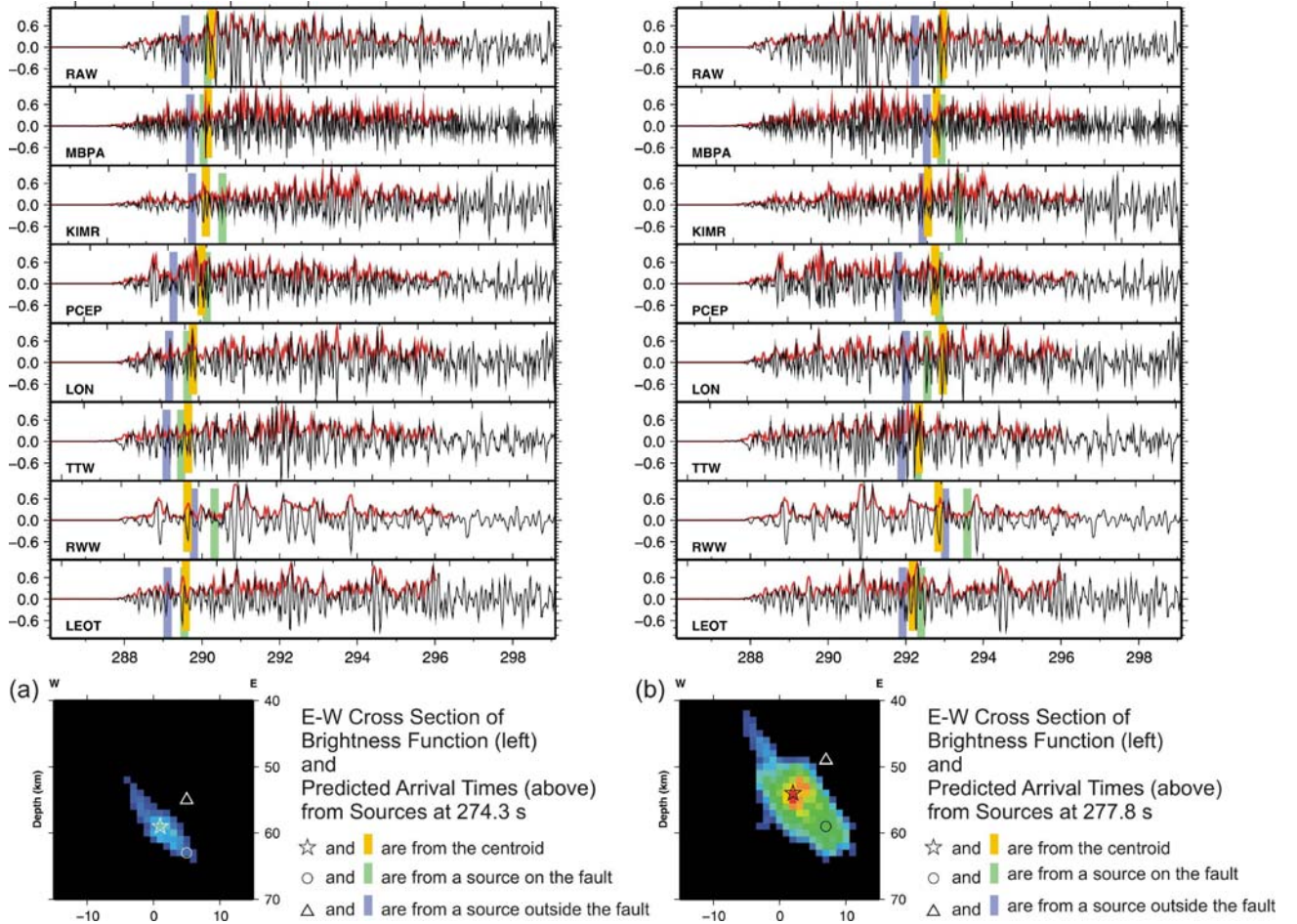


Fig. 5. Examples of forward modeling of arrival times from different point source locations (as shown in the lower panel) and comparison with observed waveforms (upper panel).

moved from the centroid location (star) to a place outside of the fault (triangle). In comparison, the drop is about 25% if it is moved to a location downdip along the east-dipping plane (circle).

We also performed finite-fault modeling using a method similar to those of previous strong-motion studies for this earthquake [Xu et al., 2002; Ichinose et al., 2004] except that the same dataset as used in our SSA analysis were used. Not surprisingly, we reached the same conclusion as the previous studies that both nodal planes give similar fit to the data such that the rupture plane cannot be identified. This result suggests that the synthetic waveform approach, as that used in finite-fault modeling, probably does not have sufficient resolution in distinguishing the fault plane from the auxiliary plane unless the magnitude of the target event is very large.

## Geophysical Implication

Wang et al. [2004a] proposed that there is a tendency for larger intraslab earthquakes to occur deeper inside the slab. They argued that rock densification during the transformation of meta-basalt into eclogite in the upper few hundred meters of the slab crust will shatter the upper crust and cause many small earthquakes to occur. Transformation and hence densification of the largely anhydrous lower crust is expected to be kinetically delayed and sluggish [Hacker et al., 2003], except locally in hydrated parts such as faults. The untransformed lower crust and the mantle are much less fractured and hence more uniform. If dehydration along hydrated existing faults triggers seismic rupture, ruptures have a better opportunity to

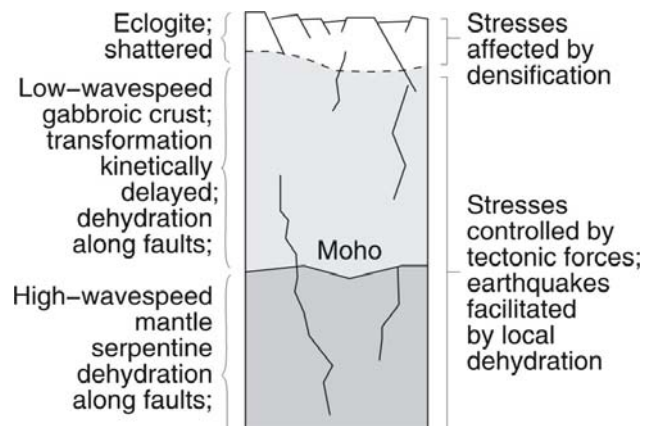


Fig. 6. Metamorphic dehydration state of a warm slab in the 30-60 km depth range. The untransformed lower crust and mantle have a similar state of stress. From Wang et al. (2004b).

propagate farther, resulting in larger earthquakes. Before the bulk of the lower crust is transformed to eclogite, there is little contrast in the state of stress between the lower crust and uppermost mantle. If a rupture is initiated in the lower crust, it may propagate downward across the slab Moho (Fig. 6), as is the case in the Geiyo and Nisqually earthquakes. The tendency for larger earthquakes to occur deeper inside the slab, i.e., in the lower crust or topmost mantle, has also been shown independently through precise relocation of Cascadia intraslab earthquakes [Cassidy and Waldhauser, 2002]. Wang et al. [2004a] further predicted that the rupture plane of the Nisqually earthquake is likely the steeply dipping one; because of the shattered state of the crust, the nearly horizontal one across the crust is unlikely.

The postulation and prediction of Wang et al. [2004a] are supported by the results of the present study. The Nisqually earthquake (Fig. 1) occurred in the dehydrating region of slab crust and topmost slab mantle. Large earthquakes occurring closer to the slab Moho, due to deserpentinization of the slab mantle and dehydration of the lower unaltered slab crust are probably not limited in size by the thickness of the slab crust. The rupture could extend from the slab crust into the slab upper mantle with large propagation distance.



## Conclusion

Physics-based approaches to earthquake hazard studies allow us to investigate important questions such as: Can Cascadia in-slab earthquakes be much larger than magnitude 7? In this project, we have addressed this issue by investigating the rupture geometry of the 2001 Nisqually earthquake thus answering the question whether the maximum size of Cascadia intraslab earthquakes is limited by the thickness of the subducting crust. Moment tensor studies have provided two candidates for the rupture plane of this earthquake (Fig. 1a). Using modified SSA, we have determined that the steeply east-dipping plane is the rupture plane. The SSA results and previous strong-motion inversion results both suggest that the rupture propagated downward and therefore must have significantly extended into the subducting mantle. Involvement of the lower crust and uppermost mantle of the subducting slab in earthquake rupture is consistent with our knowledge of the thermal and petrological states of the Cascadia slab. If intraslab earthquake ruptures are not confined in the subducting crust of 7 km thickness, the maximum size of these events may be greater than those of the 1949 Olympia earthquake (M 7.1) and the 2001 Nisqually earthquake (M 6.8).

## Appendix. Controlled Experiments Using SSA With Synthetic Data

Fig. A1 shows the configuration of our controlled studies. Two seismic arrays with different epicentral distance ranges are used in the experiments, as shown in Fig. A1a. Stations A11–A43 are located within 50 km from the centroid of the rupture plane with a spatial interval of 20–25 km along both X and Y directions. Stations C11–C55, on the other hand, are 50–150 km away from the rupture plane with an inter-station distance of about 50 km, which is a more realistic circumstance for most existing local seismic networks. The rupture plane has a horizontal radius of 6 km. Different configurations of ‘asperities’ (i.e., points where strong seismic energy is emitted) can be placed inside to mimic the various aspects of a real seismic source (Fig. A1b). For example, the source distribution is more heterogeneous if asperities are placed at larger distance from each other. The rupture propagation effect can also be simulated by delaying the origin time of each asperity according to the rupture direction and velocity. The two conjugate cases (i.e., east-dipping and west-dipping) are mimicked by adjusting the depths of all asperities with respect to the center (Fig. A1b).

For each station, we calculate synthetic seismograms corresponding to both east- and west-dipping rupture planes with a simple 1D velocity model (a 30-km crust over mantle half space). The waveform amplitude is attenuated depending on the source-station distance (i.e., the geometric spreading effect). To make our cases more realistic, a significant amount of random noise (25% of the signal amplitude) is also added during the calculation.

Fig. A1c shows the synthetic waveforms at stations C11–C35 using an inter-asperity distance of 3 km (Fig. A1b). All sources are assumed to have occurred at the same time (10 s) with the same amplitude. Because of the N–S symmetry in the source and station configurations (Figs A1a and A1b), stations C41–C45 and C51–C55 have the same waveforms as C21–25 and C11–C15, respectively. Notice that a significant difference in the waveforms exists between the two dipping cases (Fig. A1c). This is especially true for stations in the updip or downdip directions. For each waveform, the corresponding envelope is constructed by taking the root mean square of the waveform and its Hilbert transform.

We apply SSA to the waveform envelopes at stations C11–C55 and the results are shown in Fig A2. Because the two source models are symmetric with respect to  $X=0$ , we expect the SSA image of the west-dipping rupture to be a perfect flip of the east-dipping one. This is exactly the case shown in Fig. A2a, confirming that the difference in inputted waveforms can be faithfully converted into the difference in source distributions.

The derived origin time, locations, and depths of the bright spots correspond exactly to the inputted distribution of asperities shown in Fig. A1. However, we notice that not all the recovered sources show the same brightness. According to equation (3), different brightness values mean that there is a difference in the summation of observed amplitudes. In our case, this is mainly due to constructive and/or destructive interferences among wavelets originated from different asperities. For examples, the waveforms at the stations C31 and C35 show only three significant wavelets, even though there are 13 asperities in the source. As a result, many asperities receive less or no amplitude contribution from these two stations due to the interference, thus showing less brightness values (Fig. A2a).

In general, the SSA image seems to constrain each asperity's epicenter better than its depth. This resolution difference is not too surprising because seismic travel time is intrinsically more sensitive to the variation in horizontal distance. In our presented case, the depth resolution

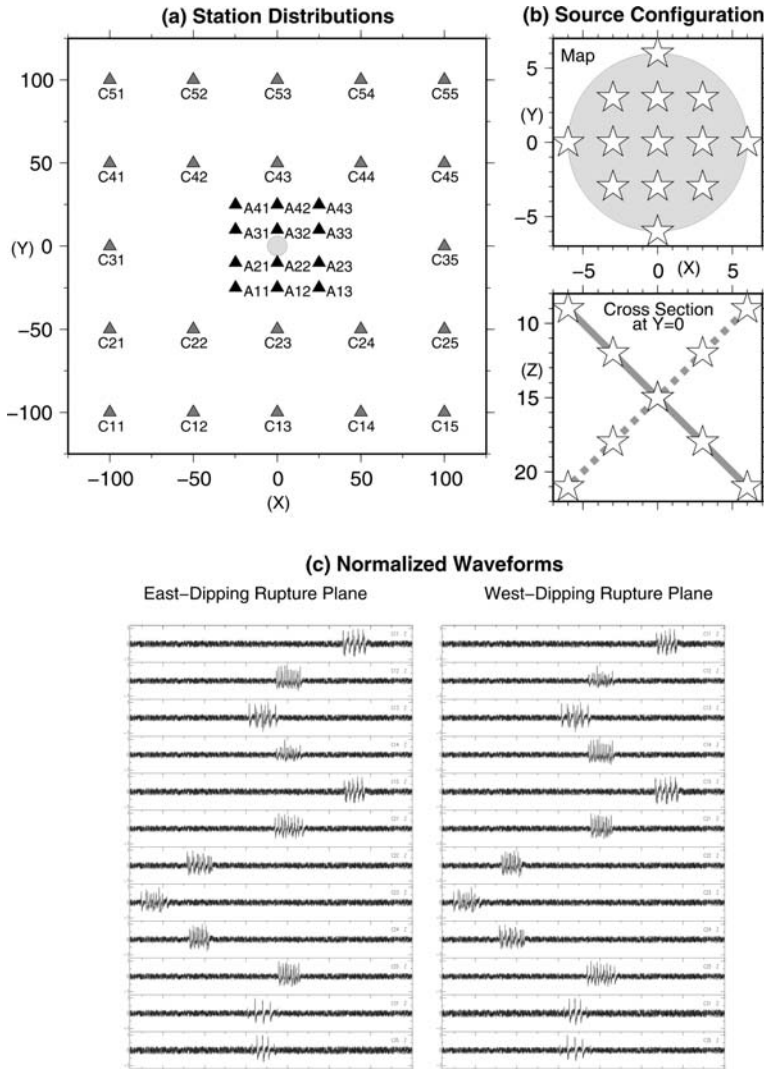


Fig. A1. Configuration of our controlled study. (a) Two seismic arrays are designed with different epicentral distance ranges. Stations A11–A43 are located within 50 km from the centroid of the rupture plane with a spatial interval of 20–25 km along both X and Y directions. Stations C11–C55 are 100–300 km away from the rupture plane with an inter-station distance of ~50 km. (b) The rupture plane has a horizontal radius of 6 km with many asperities evenly distributed inside. The inter-asperity distance is set at 3 km. The two conjugate cases (i.e., east-dipping: solid line, and west-dipping: dashed line) are mimicked by adjusting the depths of asperities. (c) Synthetic waveforms at stations C11–C35 corresponding to the east-dipping (left panel) and west-dipping (right panel) rupture planes. To make the study more realistic, a 30% level of random noise is added to each seismogram. All waveforms are normalized between 0 and 1 before calculating the brightness function.

deteriorates rapidly toward shallow depths (Fig. A2a). At a source depth of 10 km, the uncertainty can be as large as  $\pm 3$  km.

To test the robustness of our method under the presence of hypocentral mislocation and some error in the event's origin time, we introduce a set of station corrections to the calculation of brightness function such that the centroid of the rupture plane appears to be shifted slightly in both time and place. The amounts of origin time error (1.5 s) and mislocation (5 km along all three axes) are comparable to the uncertainties routinely determined by most local networks. The exact value of time correction for each station differs slightly depending on the difference between the old and new propagation paths. The range is generally within  $\pm 3$  s.

Fig. A2b shows the SSA images of an east-dipping rupture plane when the centroid is mistakenly corrected to a wrong place and time. The relative positions of all asperities can be recovered remarkably well while their absolute locations are systematically shifted. The locations and depths appear to be less resolved, though, because some neighbouring grids (especially along the vertical direction) also seem to show some brightness (Fig. A2b).

The location and depth resolution becomes even worse if waveform envelopes from stations closer to the source region (A11–A43) are used in the

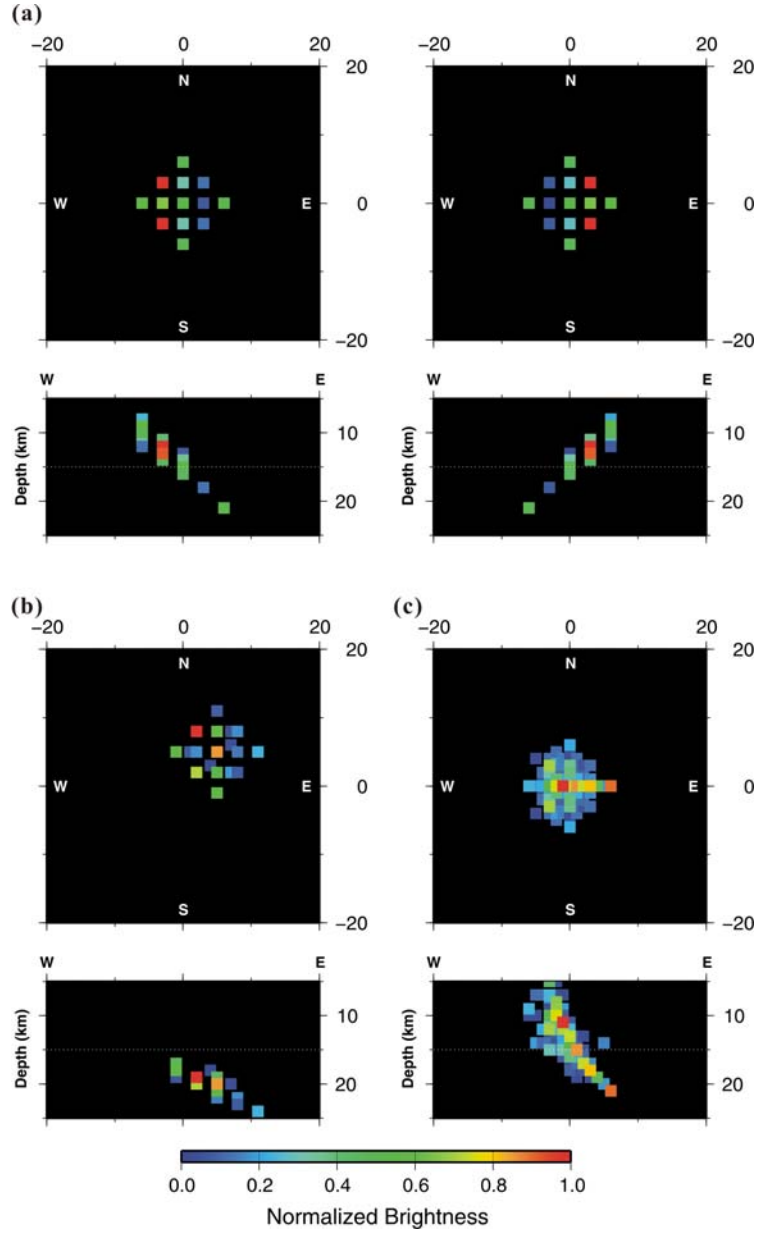


Fig. A2. Source images obtained by SSA for the controlled study shown in Fig. A1. (a) Results using waveform envelopes from stations C11-C55. The image of the west-dipping rupture (right panel) is a perfect flip of the east-dipping one (left panel), exactly as the inputted waveforms have suggested. (b) Similar to the east-dipping case in (a) but with the presence of hypocentral mislocation (5 km along each direction) and 1.5 s error in the origin time. The overall pattern of east-dipping rupture remains well recovered. (c) Similar to the east-dipping case in (a) but using waveform envelopes from stations closer to the source area (A11-A43). The resolution for individual sources becomes much worse, but the east-dipping plane is still recognizable.

SSA calculation (Fig. A2c). This is mainly due to the increasing amplitude contrast among the wavelets originated from different asperities. Taking the station A22 for example, the peak amplitude produced by the closest asperity is more than 40% larger than that by the farthest. As a result, the SSA can only map out the overall source region but not the exact locations of individual asperities. The situation is less well-resolved at shallow depths (Fig. A2c).

We repeat the experiment under a variety of different scenarios, such as using different inter-asperity distances, adding the rupture propagation effect, using time corrections that correspond to different amounts of origin time error and/or mislocation, and having different choices of controlling parameters in the calculation of brightness function. It turns out that the SSA method works best for a heterogeneous source distribution (i.e., when the inter-asperity distance is discernable). When the rupture propagation is added (by setting the origin time of each asperity slightly different), the resolution of SSA images improves slightly because the various wavelets from different asperities are farther separated in time. In all cases, the overall source pattern can be recovered and the dipping nature of the rupture plane can be confirmed beyond any doubt.

## References (those marked \* are publications from this project)

- Atkinson, G. M., and R. Casey, A comparison of ground motion from the 2001 M6.8 in-slab earthquakes in Cascadia and Japan, *Eos. Trans. AGU*, 83(47), Fall Meet. Suppl., Abstract S21C-11, 2002.
- Bustin, A., R.D. Hyndman, A. Lambert, J. Ristau, H. Dragert, and M. Van der Kooij, Fault parameters of the Nisqually earthquake determined from moment tensor solutions and the surface deformation from GPS and InSAR, *Seismological Society of America Bulletin*, in press, 2004.
- Cassidy, J. F., and F. Waldhauser, Evidence for both crustal and mantle earthquakes in the subducting Juan de Fuca plate, *Geophys. Res. Letts.*, 30(2), 1095, doi:10.1029/2002GL015511, 2003.
- Creager, K. C., L. A. Preston, Q. Xu, and R. S. Crosson, The 2001 Mw 6.8 Nisqually Earthquake: An along-strike elongated fault rupturing entirely within the subducted oceanic crust? (Abstract), *Seismol. Res. Let.*, 73, 213, 2002.
- Hacker, B. R., S. M. Peacock, G. A. Abers, and S. D. Holloway, Subduction factory 2. Are intermeditate-depth earthquakes in subducting slabs linked to metamorphic dehydration reactions? *J. Geophys. Res.*, 108(B1), 2030, doi:10.1029/2001JB001129, 2003.
- Ichinose, G. A., H. K. Thio, and P. G. Somerville (2004), Rupture process and near-source shaking of the 1965 Seattle-Tacoma and 2001 Nisqually, intraslab earthquakes, *Geophys. Res. Lett.*, 31, L10604, doi:10.1029/2004GL019668.
- Kakehi Y. (2004), Analysis of the 2001 Geiyo, Japan, earthquake using high-density strong ground motion data: Detailed rupture process of a slab earthquake in a medium with a large velocity contrast, *J. Geophys. Res.*, 109, B08306, doi:10.1029/2004JB002980.
- Kirby, S. H., E. R. Engdahl, and R. Denlinger, Intermediate-depth intraslab earthquakes and arc volcanism as physical expressions of crustal and uppermost mantle metamorphism in subducting slabs, in *Subduction: Top to Bottom*, AGU Monograph 96, edited by G. E. Bebout, D. W. Scholl, S. H. Kirby, and J. P. Platt, AGU, Washington DC, pp.195-214, 1996.
- Kao, H., and S. Shan, The Source-Scanning Algorithm: Mapping the Distribution of Seismic Sources in Time and Space, *Geophys. J. Int.*, 157, 589-594, 2004.

- \*Kao, H., and S. Shan (2006), Rapid identification of earthquake rupture plane using Source-Scanning Algorithm, *Geophys. J. Int.*, in press.
- \*Kao, H., K. Wang, and R.-Y. Chen (2006), Identifying the rupture plane of 2001 Nisqually, Washington earthquake and implications to seismic hazards in northern Cascadia, to be submitted to *Nature*.
- Ohkura, T., and T. Seno, Did Geoyo earthquake (2001.3.24) occur in the slab mantle? (in Japanese), Abstracts of Seismological Society of Japan Fall Meeting, A64, 2002.
- Peacock, S. M., and K. Wang, Seismic consequences of warm versus cool subduction metamorphism: Examples from Southwest and Northeast Japan, *Science*, 286, 937-939, 1999.
- Preston, L. A., K. C. Creager, R. S. Crosson, T. M. Brocher, and A. M. Trehu, Intralab Earthquakes: Dehydration of the Cascadia Slab, *Science*, 302, 1197-1200, 2003.
- Stöckhert, B., and J. Renner, Rheology of crustal rocks at ultrahigh pressure, in *When Continents Collide: Geodynamics and Geochemistry of Ultrahigh-pressure rocks*, edited by B. R. Hacker and J. G. Liou, Kluwer Academic, Amsterdam, 1998.
- Wang, K., J. C. Cassidy, I. Wada, and A. J. Smith, Effects of metamorphic crustal densification on earthquake size in warm slabs, *Geophys. Res. Lett.*, 108(B1), 2026, doi:10.1029/2001JB001227, 2004a.
- Wang, K., I. Wada, and Y. Ishikawa, Stresses in the subducting slab beneath Southwest Japan and relation with plate geometry, tectonic forces, slab dehydration, and damaging earthquakes, *J. Geophys. Res.*, submitted, 2004b.
- Xu, Q., K. C. Creager, and R. S. Crosson, Rupture history of the 2001 Nisqually, Washington earthquake (Abstract), *Seismol. Res. Lett.*, 73, 213, 2002.